

## Article

# Boosted Catalytic Activity toward the Hydrolysis of Ammonia Borane by Mixing Co- and Cu-Based Catalysts

Jinyun Liao <sup>1,2,†</sup>, Yujie Wu <sup>1,†</sup>, Yufa Feng <sup>2</sup>, Haotao Hu <sup>2</sup>, Lixuan Zhang <sup>2</sup>, Jingchun Qiu <sup>2</sup>, Junhao Li <sup>1</sup>, Quanbing Liu <sup>1,\*</sup> and Hao Li <sup>2,\*</sup>

<sup>1</sup> School of Chemical Engineering and Light Industry, Guangdong University of Technology, Guangzhou 510006, China; jyliao@126.com (J.L.); 2112006114@mail2.gdut.edu.cn (Y.W.); 1112006009@mail2.gdut.edu.cn (J.L.)

<sup>2</sup> Guangdong Provincial Key Laboratory for Electronic Functional Materials and Devices, School of Chemistry and Materials Engineering, Huizhou University, Huizhou 516007, China; yufafeng@126.com (Y.F.); huhaotao5182@163.com (H.H.); z15728482326@163.com (L.Z.); qjc1006863526@163.com (J.Q.)

\* Correspondence: liuqb@gdut.edu.cn (Q.L.); lihao180@126.com (H.L.); Tel.: +86-752-2527229 (H.L.)

† These authors contributed equally to this work.

**Abstract:** Promoting the activity of heterogeneous catalysts in the hydrolysis of ammonia borane for hydrogen production is still a challenging topic for researchers in the hydrogen energy and catalysis fields. Herein, we present a universal, simple and efficient strategy to boost the catalytic performance toward AB hydrolysis by mixing Co- and Cu-based catalysts for the first time. Synergistic catalysts with remarkably enhanced activity can be obtained by mixing a Co-based catalyst and a Cu-based catalyst together, such as  $\text{Co}_3\text{O}_4$  and  $\text{Cu}_3(\text{MoO}_4)_2(\text{OH})_2$ ,  $\text{Co}_3\text{O}_4$  and  $\text{Cu}_3(\text{PO}_4)_2$ ,  $\text{Co}_3(\text{PO}_4)_2$  and  $\text{Cu}_3(\text{MoO}_4)_2(\text{OH})_2$ ,  $\text{Co}_3(\text{PO}_4)_2$  and  $\text{Cu}_3(\text{PO}_4)_2$ , and  $\text{CuO}$  and  $\text{Co}_3\text{O}_4$ . For example, the turnover frequency (TOF) for the mixture catalyst of  $\text{Co}_3\text{O}_4$  and  $\text{Cu}_3(\text{MoO}_4)_2(\text{OH})_2$  with a mass ratio of 4:1 is up to  $77.3 \text{ min}^{-1}$ , which is approximately 11.5 times higher than that of the sum of  $\text{Co}_3\text{O}_4$  and  $\text{Cu}_3(\text{MoO}_4)_2(\text{OH})_2$ . The reasons for these findings are discussed in detail. The observations and conclusions in this work may provide a guideline for promoting the hydrolysis of ammonia borane through a simple and effective approach.

**Keywords:** hydrogen production; ammonia borane; heterogeneous catalysis; physical mixture; synergistic effect



**Citation:** Liao, J.; Wu, Y.; Feng, Y.; Hu, H.; Zhang, L.; Qiu, J.; Li, J.; Liu, Q.; Li, H. Boosted Catalytic Activity toward the Hydrolysis of Ammonia Borane by Mixing Co- and Cu-Based Catalysts. *Catalysts* **2022**, *12*, 426. <https://doi.org/10.3390/catal12040426>

Academic Editor: Keith Hohn

Received: 15 February 2022

Accepted: 31 March 2022

Published: 11 April 2022

**Publisher's Note:** MDPI stays neutral with regard to jurisdictional claims in published maps and institutional affiliations.



**Copyright:** © 2022 by the authors. Licensee MDPI, Basel, Switzerland. This article is an open access article distributed under the terms and conditions of the Creative Commons Attribution (CC BY) license (<https://creativecommons.org/licenses/by/4.0/>).

## 1. Introduction

Energy crises and environmental issues have hindered economic development in the past several decades and continue to do so today; thus, it is urgently required to find a green and renewable energy source to substitute traditional fossil fuel energy sources with carbon-neutral sources [1,2]. Hydrogen energy is one of the best carbon-neutral alternatives to fossil fuel energy due to its high gravimetric energy density and zero pollution. However, how to transport and store hydrogen in an efficient and safe manner is a crucial issue that needs to be well-addressed before its large-scale applications. Therefore, many efforts have been made to develop strategies for hydrogen storage and transportation. Compared with the physical approach to hydrogen storage, chemical hydrogen storage is considered more effective and safer. Ammonia borane, with the formula  $\text{NH}_3\text{BH}_3$ , has attracted extensive attention because of its non-toxicity, high hydrogen content of 19.6 wt% and good stability under ambient temperature [3]. Additionally, due to its mild reaction conditions and environmental friendliness, hydrogen production from  $\text{NH}_3\text{BH}_3$  using hydrolysis is more attractive compared with pyrolysis and solvolysis.

However, since  $\text{NH}_3\text{BH}_3$  hydrolysis is kinetically unfeasible in the absence of a catalyst, a robust catalyst is indispensable for this hydrolytic reaction [4]. In the past, it was reported

that noble-metal-based catalysts were quite active to  $\text{NH}_3\text{BH}_3$  hydrolysis [5–7]. However, due to its high cost, it is difficult to use noble metals or their alloys as catalysts to  $\text{NH}_3\text{BH}_3$  hydrolysis on an industrial scale. Meanwhile, the non-precious-metal-based catalysts have attracted great interest due to their low cost [8–10]. However, the activity of non-precious-metal-based catalysts is still not satisfactory. Therefore, in recent years, researchers have undertaken a serious effort to improve the activity of non-precious-metal-based catalysts, and many strategies have been proposed. Among them, there are three commonly used strategies to boost the activity of the catalysts, namely, dispersing the active species on proper supports, compositing different active species together to form hybrid catalysts and controlling the morphology of nanocatalysts. Taking advantage of the first strategy, Feng et al. successfully dispersed  $\text{Cu}_x\text{Co}_{1-x}\text{O}$  nanoparticles on graphene, which remarkably enhanced the performance of the catalyst in promoting  $\text{NH}_3\text{BH}_3$  hydrolysis with a turnover frequency (TOF) value of  $70.0 \text{ min}^{-1}$  [11]. They ascribed the enhancement of the catalytic activity of the hybrid to the interfacial interaction between the nanoparticles and the graphene. There are also some successful examples for the second strategy. In our previous work [12], we fabricated  $\text{Co}_{0.8}\text{Cu}_{0.2}\text{MoO}_4$  composite microspheres and found that their catalytic activity was much higher than that of  $\text{CoMoO}_4$  and  $\text{CuMoO}_4$ , indicating that the reactivity of the catalyst could be remarkably improved by compositing  $\text{CoMoO}_4$  and  $\text{CuMoO}_4$ . The third strategy is based on the effect of the morphology of nanocatalysts. For example, Yamada et al. have successfully synthesized  $\text{Co}_3\text{O}_4$  consisting of particles, cube and sheet, and compared their catalytic activity toward AB hydrolysis [13]. Their results demonstrated that  $\text{Co}_3\text{O}_4$  exhibits a morphology-dependent catalytic performance. By tuning the morphology, the activity of the catalyst can be significantly enhanced.

Although the above-mentioned strategies can be applied to obtain high-performance catalysts for AB hydrolysis, the synthetic processes are often tedious, costly, or both. Additionally, these catalysts must be intricately designed and synthesized to ensure their high reactivity. For example, nanocatalysts with different morphology may exhibit different catalytic behavior. However, it is not easy to predict which kind of shape-anisotropic nanocatalysts can exhibit the highest catalytic performance and how to design and synthesize them. Thus, although highly desirable, it is still challenging to develop an economical, simple and universal method to boost the catalytic activity of inexpensive catalysts that can be easily applied in practice on a large scale. In this study, we propose a simple method to produce low-cost mixture catalysts with remarkably boosted catalytic performance toward AB hydrolysis based on mixing Co- and Cu-based compounds. First, we successfully synthesized  $\text{Co}_3\text{O}_4$ ,  $\text{Co}_3(\text{PO}_4)_2$ ,  $\text{Cu}_3(\text{PO}_4)_2$ ,  $\text{CuO}$  and  $\text{Cu}_3(\text{MoO}_4)_2(\text{OH})_2$ . Then, we mixed these Co- and Cu-based compounds in an arbitrary, trial-and-error manner, and synergistic mixture catalysts were obtained in this way. In particular, by controlling the mass ratio of Co- and Cu-based compounds, high-performance catalysts can be obtained. Note that  $\text{Co}_3(\text{PO}_4)_2$  and  $\text{Cu}_3(\text{PO}_4)_2$  were selected because their hybrids exhibit good catalytic activity in AB hydrolysis [14]. As we know, there has not yet been a report describing the production of high-performance synergistic catalysts towards AB hydrolysis by physically mixing two low-cost compounds. These findings provide a guideline for promoting  $\text{NH}_3\text{BH}_3$  hydrolysis by a simple and effective approach.

## 2. Results and Discussion

The SEM images and XRD patterns of  $\text{Co}_3\text{O}_4$  and  $\text{Cu}_3(\text{MoO}_4)_2(\text{OH})_2$  are shown in Figure 1a–f. The SEM images of  $\text{Co}_3\text{O}_4$  (Figure 1a,b) reveal that our sample of  $\text{Co}_3\text{O}_4$  consists of uniform microspheres with a diameter of ca. 500–1000 nm. The magnified SEM image of the  $\text{Co}_3\text{O}_4$  (Figure 1b) clearly shows that it is composed of numerous nanoparticles with a size of about 80 nm. The sample surface is very coarse, and thus has a large specific surface area. The XRD pattern of  $\text{Co}_3\text{O}_4$ , displayed in Figure 1e, shows all the characteristic peaks of  $\text{Co}_3\text{O}_4$  (JCPDS 42-1467), and no other peaks associated with impurity appear, indicating that the sample is pure  $\text{Co}_3\text{O}_4$ . The morphology of  $\text{Cu}_3(\text{MoO}_4)_2(\text{OH})_2$ , displayed in Figure 1c,d, reveals that the  $\text{Cu}_3(\text{MoO}_4)_2(\text{OH})_2$  sample consists of an aggregated nanoplate

with a mean thickness of ca. 120 nm. The XRD pattern of  $\text{Cu}_3(\text{MoO}_4)_2(\text{OH})_2$ , shown in Figure 1f, matches well with the standard pattern of  $\text{Cu}_3(\text{MoO}_4)_2(\text{OH})_2$  (JCPDS 36-0405). The SEM images and XRD patterns of  $\text{Cu}_3(\text{PO}_4)_2 \cdot 3\text{H}_2\text{O}$ ,  $\text{CuO}$  and  $\text{Co}_3(\text{PO}_4)_2$  are presented in Figure S2a–i in the Supplementary Materials. The SEM images clearly show that the sphere-shaped  $\text{Co}_3(\text{PO}_4)_2$  particles (Figure S2a,b) are uniformly distributed with a diameter of ca. 500 nm. The XRD pattern shows no obvious peaks of  $\text{Co}_3(\text{PO}_4)_2$  (Figure S2c), which indicates the obtained  $\text{Co}_3(\text{PO}_4)_2$  is in an amorphous state. In order to further confirm the structure of  $\text{Co}_3(\text{PO}_4)_2$ , an FTIR spectroscopy analysis was performed on the sample. The result, shown in Figure S3, revealed two obvious peaks in the fingerprint region with wavenumbers of 590.3 and 1043.4  $\text{cm}^{-1}$ , which are indexed to the vibration of Co-O and  $(\text{PO}_4)^{3-}$  in  $\text{Co}_3(\text{PO}_4)_2$ , respectively [15]. It is evident that the morphology of  $\text{CuO}$  is rod-shaped with an average diameter of 80 nm (Figure S2d,e), and such rod-shaped  $\text{CuO}$  particles are uniformly distributed without aggregation. The XRD pattern, shown in Figure S2f, indicates that the phase of our product is monoclinic  $\text{CuO}$  (JCPDS 45-0937). The microstructures of  $\text{Cu}_3(\text{PO}_4)_2 \cdot 3\text{H}_2\text{O}$ , shown in Figure S2g,h, clearly indicate that the obtained  $\text{Cu}_3(\text{PO}_4)_2 \cdot 3\text{H}_2\text{O}$  is uniformly distributed with a three-dimensional (3D) hierarchical flower-like porous structure, which is composed of numerous interconnected nanosheets. The magnified SEM image (Figure S2h) reveals that the thickness of those nanosheets is about 60 nm. The XRD pattern of the  $\text{Cu}_3(\text{PO}_4)_2 \cdot 3\text{H}_2\text{O}$  sample, displayed in Figure S2i, matches well with the standard pattern of  $\text{Cu}_3(\text{PO}_4)_2 \cdot 3\text{H}_2\text{O}$  (JCPDS 22-0548), indicating that our sample is  $\text{Cu}_3(\text{PO}_4)_2 \cdot 3\text{H}_2\text{O}$  instead of anhydrous  $\text{Cu}_3(\text{PO}_4)_2$ .

The TEM images of  $\text{Co}_3\text{O}_4$  and  $\text{Cu}_3(\text{MoO}_4)_2(\text{OH})_2$ , displayed in Figure 2, show that the size of the  $\text{Co}_3\text{O}_4$  microsphere is about 700 nm, which coincides with the SEM result. In addition, the inner core of the  $\text{Co}_3\text{O}_4$  microsphere has a hollow interior structure with a cage size of ca. 250 nm. The formation of the hollow structure may be related to the agglomeration of the nanoparticles. The nanocrystal subunits on the surface of  $\text{Co}_3\text{O}_4$  particles are displayed in the HRTEM image (Figure 2b), with interplanar spaces of 0.24, 0.47 and 0.29 nm, which are associated with the (311), (111) and (220) lattice planes of cubic  $\text{Co}_3\text{O}_4$ , respectively. The TEM and HRTEM images of  $\text{Cu}_3(\text{MoO}_4)_2(\text{OH})_2$ , displayed in Figure 2c,d, show that  $\text{Cu}_3(\text{MoO}_4)_2(\text{OH})_2$  has a nanoplate morphology with a smooth surface, and the thickness of the obtained product is about 120 nm. The lattice fringe spacing of the sample was determined to be about 0.43 nm and was ascribed to the (021) lattice plane of monoclinic  $\text{Cu}_3(\text{MoO}_4)_2(\text{OH})_2$ . The functional groups in the  $\text{Co}_3\text{O}_4$  and  $\text{Cu}_3(\text{MoO}_4)_2(\text{OH})_2$  catalysts were analyzed with FTIR. The spectra of  $\text{Co}_3\text{O}_4$  and  $\text{Cu}_3(\text{MoO}_4)_2(\text{OH})_2$ , displayed in Figure 2e, show absorption bands centered at 3429, 1639 and 2360  $\text{cm}^{-1}$ , which are ascribed to the symmetrical/antisymmetric stretching vibration of free water molecules adsorbed on the surface of the catalysts, the bending vibration of HO-H, and the vibration of adsorbed atmospheric  $\text{CO}_2$ , respectively [16]. Additionally, in the fingerprint region of  $\text{Co}_3\text{O}_4$ , the two strong absorption bands centered at 663 and 567  $\text{cm}^{-1}$  are related to the vibration of  $\text{Co}^{2+}\text{-O}^{2-}$  and  $\text{Co}^{3+}\text{-O}^{2-}$  [16]. In the spectrum of the  $\text{Cu}_3(\text{MoO}_4)_2(\text{OH})_2$ , the absorption bands centered at 962.5  $\text{cm}^{-1}$  are indexed to the  $\nu_1$  vibration of distorted  $\text{MoO}_4$  in  $\text{Cu}_3(\text{MoO}_4)_2(\text{OH})_2$  [17]. In addition, the bands present at 916.2 and 821.6  $\text{cm}^{-1}$  can be attributed to the symmetric stretching and asymmetric stretching vibrations of the Mo-O-Mo [18]. The band centered at 453.3  $\text{cm}^{-1}$  is related to the Cu-OH vibration in  $\text{Cu}_3(\text{MoO}_4)_2(\text{OH})_2$  [19]. The FTIR spectra of  $\text{CuO}$  and  $\text{Cu}_3(\text{PO}_4)_2$  are presented in Figure S3. In the  $\text{CuO}$  FTIR spectrum, displayed in Figure S3b, the three strong bands appearing at 420.5, 532.3 and 603.7  $\text{cm}^{-1}$  can be associated with the Cu-O vibration of  $\text{CuO}$  [20]. In the fingerprint region of the  $\text{Cu}_3(\text{PO}_4)_2$  FTIR spectrum, displayed in Figure S3c, the bands located at 1149  $\text{cm}^{-1}$  can be attributed to the  $p = \text{O}$  stretching vibration. Additionally, the bands at 1047.3, 989.5 and 630.7  $\text{cm}^{-1}$  are attributed to the vibration of the asymmetrical stretching of the P-O bond, the stretching vibration of the P-O bond and the bending vibration of the P-O bond, respectively. The absorption bands at 561.3  $\text{cm}^{-1}$  are indexed to the in-plane bending vibration of the phosphate ion, and the bands present at 408.9  $\text{cm}^{-1}$  are indexed to the vibration of the Cu-O band. The

FTIR spectroscopy analysis result of the as-obtained  $\text{Cu}_3(\text{PO}_4)_2$  matches with that in the literature [21].

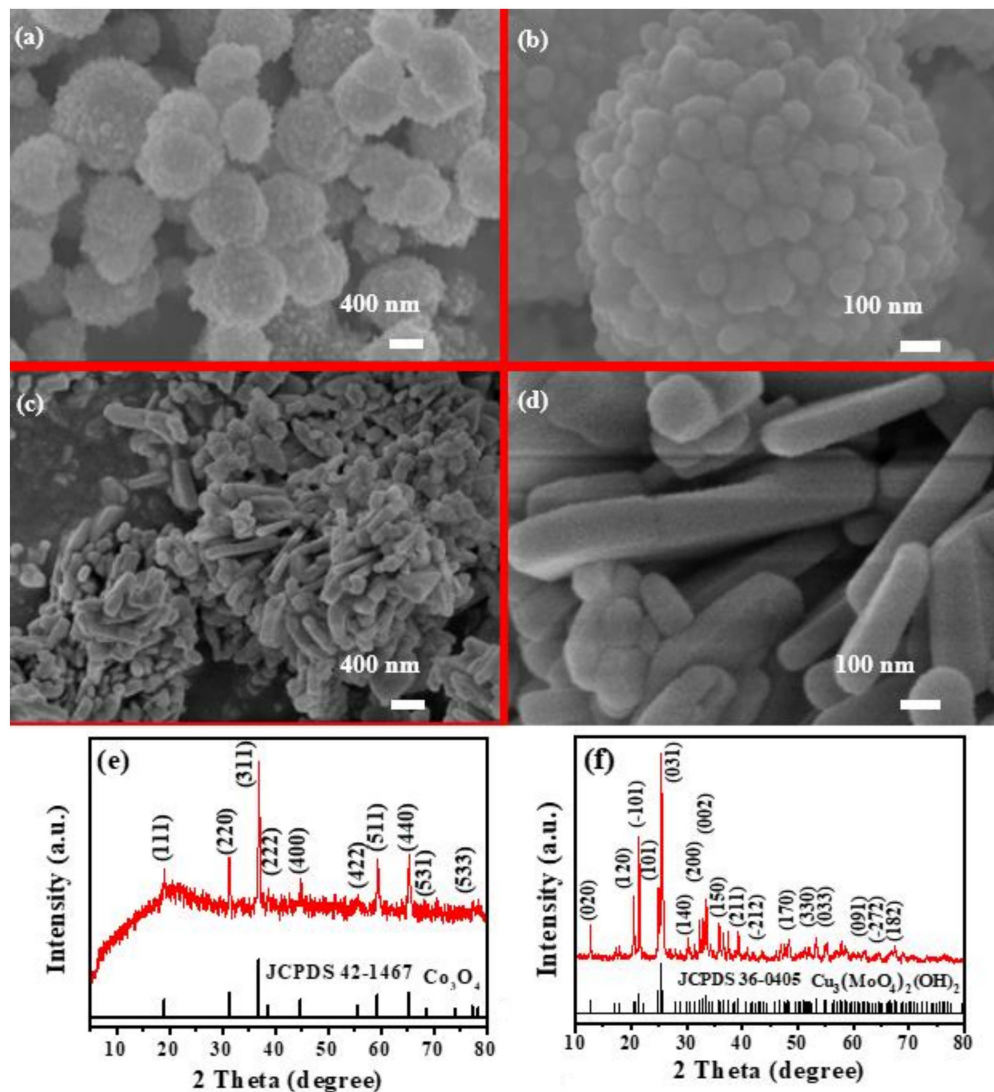


**Figure 1.** SEM images (a–d), and XRD pattern (e) of  $\text{Co}_3\text{O}_4$ , and XRD pattern (f) of  $\text{Cu}_3(\text{MoO}_4)_2(\text{OH})_2$ .

The  $\text{N}_2$  adsorption–desorption isotherms of  $\text{Co}_3\text{O}_4$  and  $\text{Cu}_3(\text{MoO}_4)_2(\text{OH})_2$ , shown in Figure 2f, clearly reveal that both compounds have a typical hysteresis loop, which exhibits a type IV isotherm, further confirming the mesoporous structure of the material. The as-synthesized  $\text{Co}_3\text{O}_4$  possesses a large BET surface area of  $99.0 \text{ m}^2/\text{g}$ , which may be related to the coarse surface and hollow microstructures of  $\text{Co}_3\text{O}_4$ . The  $\text{Cu}_3(\text{MoO}_4)_2(\text{OH})_2$  nanoplates have a relatively smaller BET surface than  $\text{Co}_3\text{O}_4$ , which is only  $6.8 \text{ m}^2/\text{g}$ . For comparison, the  $\text{N}_2$  adsorption–desorption isotherms and BET surface data of  $\text{CuO}$ ,  $\text{Co}_3(\text{PO}_4)_2$  and  $\text{Cu}_3(\text{PO}_4)_2$  are displayed in Figure S4.

XPS analysis of the catalysts was performed to know the electronic structure and valence of  $\text{Co}_3\text{O}_4$  and  $\text{Cu}_3(\text{MoO}_4)_2(\text{OH})_2$  surface. The valence of the Co element in  $\text{Co}_3\text{O}_4$  was further analyzed in Figure 2g, which reveals two major peaks at 794.7 and 779.5 eV, attributed to  $\text{Co}2\text{p}_{1/2}$  and  $\text{Co}2\text{p}_{3/2}$ , respectively. Notably, the gap between the two peaks is 15.2 eV, which further establishes the typical characteristic of  $\text{Co}_3\text{O}_4$  phase [22]. Two deconvoluted peaks with a binding energy at 796.1 and 794.6 eV are observable in the  $\text{Co}2\text{p}_{1/2}$  region, which can be assigned to  $\text{Co}^{2+}$  and  $\text{Co}^{3+}$ , respectively. In the  $\text{Co}2\text{p}_{3/2}$  region, the deconvoluted peaks at 781.1 and 779.5 eV correspond to  $\text{Co}^{2+}$  and  $\text{Co}^{3+}$ , respectively. The peaks at 804.2 and 789.1 eV are satellite peaks (Sat.) of  $\text{Co}2\text{p}$  [23]. All these peaks

are in good agreement with a previous report [23]. Four peaks are observable in the XPS spectrum of Cu2p for  $\text{Cu}_3(\text{MoO}_4)_2(\text{OH})_2$  (Figure 2h). Two of them, marked as Sat. at 962.0 and 942.3 eV, are the satellite peaks of Cu2p [23]. The other two peaks, with a binding energy at 954.3 and 934.5 eV, are attributed to  $\text{Cu}^{2+}$  in the  $\text{Cu}2\text{p}_{1/2}$  and  $\text{Cu}2\text{p}_{3/2}$  regions, respectively [23]. In the XPS spectrum of Mo3d, the two peaks appearing at 235.5 and 232.3 eV can be assigned to  $\text{Mo}^{6+}$  [12].

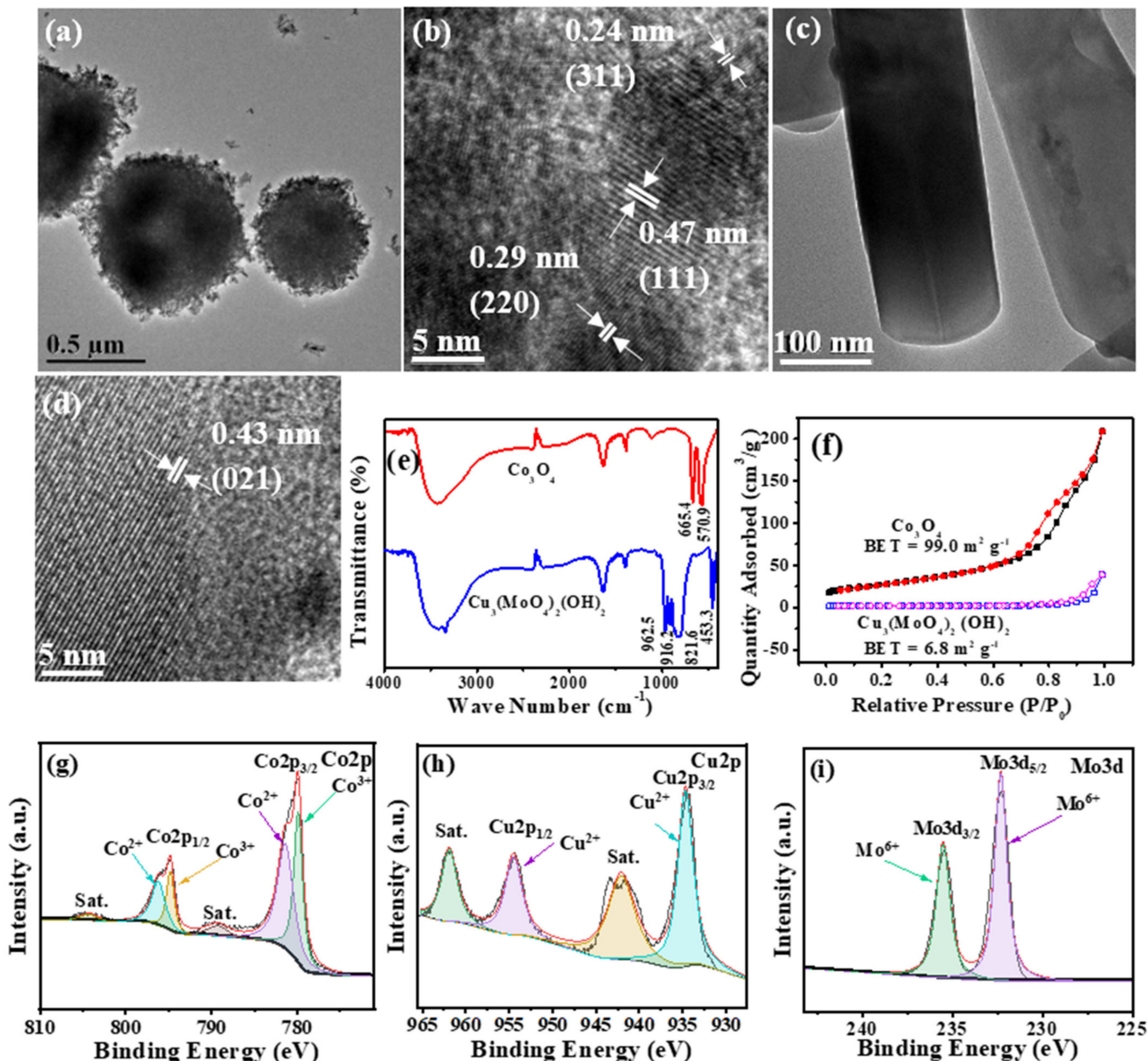


**Figure 2.** TEM and high-resolution TEM images of  $\text{Co}_3\text{O}_4$  (a,b) and  $\text{Cu}_3(\text{MoO}_4)_2(\text{OH})_2$  (c,d); FT-IR spectra of  $\text{Co}_3\text{O}_4$  and  $\text{Cu}_3(\text{MoO}_4)_2(\text{OH})_2$  (e);  $\text{N}_2$  adsorption–desorption isotherms of  $\text{Co}_3\text{O}_4$  and  $\text{Cu}_3(\text{MoO}_4)_2(\text{OH})_2$  (f); high-resolution XPS spectra of  $\text{Co}2\text{p}$  (g) of  $\text{Co}_3\text{O}_4$  and  $\text{Cu}2\text{p}$  (h),  $\text{Mo}3\text{d}$  (i) of  $\text{Cu}_3(\text{MoO}_4)_2(\text{OH})_2$ .

The catalytic activity toward AB hydrolysis of those Co- and Cu-based catalysts, shown in Figure 3a, indicates that all the catalysts are active for  $\text{NH}_3\text{BH}_3$  hydrolysis. Clearly, the Co-based compound catalysts exhibit higher activity than their Cu-based counterparts. It should be noted that, for the Co-based catalysts, there is an undesirable induction period (220 s for  $\text{Co}_3\text{O}_4$ , 130 s for  $\text{Co}_3(\text{PO}_4)_2$ ), when no hydrogen is produced. In contrast

to Co-based catalysts, Cu-based catalysts can react with AB immediately, which is superior to Co-based catalysts in terms of the reduced induction time. However, Cu-based catalysts generally show poor activity compared to Co-based catalysts, which cannot be ignored when acting as catalysts. The TOF values, which represent the catalytic activity, are calculated and compared in Figure 3b. The TOF values follow the order of:  $\text{Co}_3(\text{PO}_4)_2 > \text{Co}_3\text{O}_4 > \text{Cu}_3(\text{MoO}_4)_2(\text{OH})_2 > \text{Cu}_3(\text{PO}_4)_2 \cdot 3\text{H}_2\text{O} > \text{CuO}$ . Considering that the TOF value of  $\text{Co}_3(\text{PO}_4)_2$  is the highest among these catalysts,  $\text{Co}_3(\text{PO}_4)_2$  was characterized with XPS, EDS-mapping and H<sub>2</sub>-TPR, and the results are shown in Figure S5. Note that these five catalysts possess different surface areas (please see Figures 2f and S4). If the BET surface areas are taken into consideration, the BET surface areas normalized catalytic activity following the order of:  $\text{Cu}_3(\text{MoO}_4)_2(\text{OH})_2 > \text{Co}_3(\text{PO}_4)_2 > \text{Co}_3\text{O}_4 > \text{Cu}_3(\text{PO}_4)_2 > \text{CuO}$ .

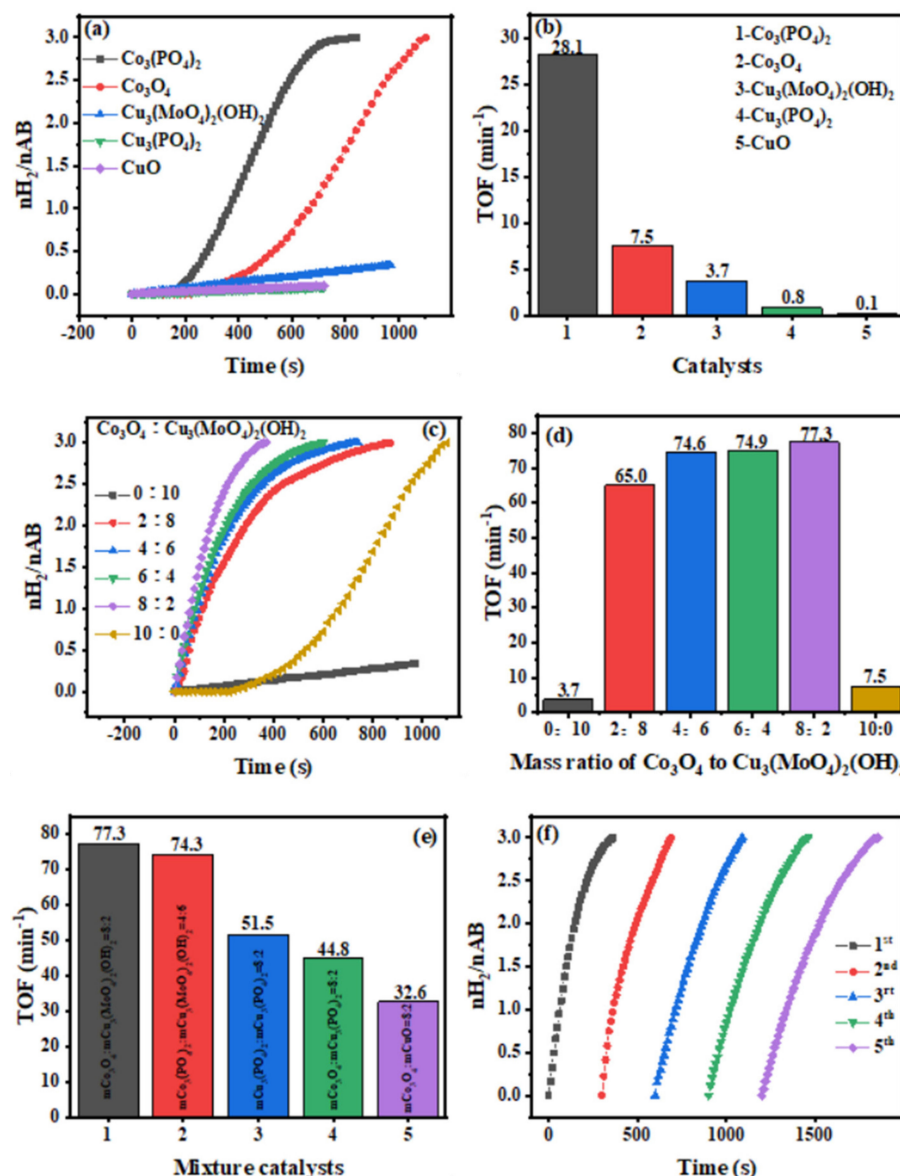


**Figure 3.** Catalytic activity of single Co-based and Cu-based catalysts (a) and their corresponding TOF values (b); catalytic performance of  $\text{Co}_3\text{O}_4$  and  $\text{Cu}_3(\text{MoO}_4)_2(\text{OH})_2$  at various mass ratios (c) and their corresponding TOF values (d); the best activity of mixture catalysts of such Co-based and Cu-based compounds with their optimal mass ratios (e) and the reusability of the mixture catalyst of  $\text{Co}_3\text{O}_4$  and  $\text{Cu}_3(\text{MoO}_4)_2(\text{OH})_2$  with a mass ratio of 8:2 (f).

The catalytic performance of all the single-component catalysts is not high in AB hydrolysis; thus, we tested the catalytic behavior of a mixture of Cu-based and Co-based compounds. To our surprise, an unexpected synergistic effect was observed when the mixture was used as a catalyst with an arbitrary mass ratio, as shown in Figures 3c and S6a–h. Specifically, Figure 3c shows the hydrogen release curves when the mixture of  $\text{Co}_3\text{O}_4$  and  $\text{Cu}_3(\text{MoO}_4)_2(\text{OH})_2$  was used as a catalyst at various mass ratios. These curves reveal that hydrogen generation is significantly improved in the presence of the mixture catalyst, without an induction period. The TOF values for the mixture catalysts of  $\text{Co}_3\text{O}_4$  and  $\text{Cu}_3(\text{MoO}_4)_2(\text{OH})_2$  at various mass ratios are shown in Figure 3d. Importantly, the TOF value reaches  $77.3 \text{ min}^{-1}$  when the mass ratio of  $\text{Co}_3\text{O}_4$  and  $\text{Cu}_3(\text{MoO}_4)_2(\text{OH})_2$  is 8:2, while those for single  $\text{Co}_3\text{O}_4$  and  $\text{Cu}_3(\text{MoO}_4)_2(\text{OH})_2$  are only  $7.5$  and  $3.7 \text{ min}^{-1}$ , respectively. The TOF value for the mixture is about 11.5 times higher than the sum of those for  $\text{Co}_3\text{O}_4$  and  $\text{Cu}_3(\text{MoO}_4)_2(\text{OH})_2$  individually. The hydrogen release curves for other mixture catalysts ( $\text{Co}_3\text{O}_4$  and  $\text{Cu}_3(\text{PO}_4)_2 \cdot 3\text{H}_2\text{O}$ ,  $\text{Co}_3\text{O}_4$  and  $\text{CuO}$ ,  $\text{Co}_3(\text{PO}_4)_2$  and  $\text{Cu}_3(\text{MoO}_4)_2(\text{OH})_2$ , and  $\text{Co}_3(\text{PO}_4)_2$  and  $\text{Cu}_3(\text{PO}_4)_2 \cdot 3\text{H}_2\text{O}$ ) with different mass ratios are shown in Figure S6a–h. All these results indicate that catalytic activity can be markedly enhanced after the Co-based and Cu-based compounds are physically mixed. Figure 3e displayed the best TOF value, corresponding to the mixture catalysts of such Co-based and Cu-based compounds with their optimal ratios. For comparison, we list the TOF values of some non-noble-metal-based catalysts in Table 1, which show that our mixture catalyst is one of the most robust catalysts in terms of its high TOF value.

**Table 1.** TOF values of some representative non-noble-metal-based catalysts toward AB hydrolysis.

| Catalysts   | TOF( $\text{molH}_2 \cdot \text{mol}_{\text{cat.}}^{-1} \cdot \text{min}^{-1}$ ) | Conditions   | Ref.      |
|---|--|--|-----------|
| $\text{Cu}_{0.6}\text{Ni}_{0.4}\text{Co}_2\text{O}_4$ nanowires   | 119.5  | $T = 298 \text{ K}, n_{\text{AB}} = 3 \text{ mmol}, M_{\text{cat.}} = 5 \text{ mg}$            | [24]      |
| $\text{Co}_x\text{Cu}_{1-x}\text{Co}_2\text{O}_4 @ \text{Co}_y\text{Cu}_{1-y}\text{Co}_2\text{O}_4$ yolk-shell microspheres | 81.8   | $T = 298 \text{ K}, n_{\text{AB}} = 3 \text{ mmol}, M_{\text{cat.}} = 10 \text{ mg}$           | [25]      |
| $\text{Ni}_{0.5}\text{Cu}_{0.5}\text{Co}_2\text{O}_4$ nanoplatelets   | 80.2   | $T = 298 \text{ K}, n_{\text{AB}} = 3 \text{ mmol}, M_{\text{cat.}} = 5 \text{ mg}$            | [16]      |
| $\text{Co}_3\text{O}_4$ and $\text{Cu}_3(\text{MoO}_4)_2(\text{OH})_2$ mixture  | 77.3   | $T = 298 \text{ K}, n_{\text{AB}} = 3 \text{ mmol}, M_{\text{cat.}} = 10 \text{ mg}$           | This work |
| $\text{CuCo}_2\text{O}_4$ nanoplatelets   | 73.4   | $T = 298 \text{ K}, n_{\text{AB}} = 2.6 \text{ mmol}, M_{\text{cat.}} = 10 \text{ mg}$         | [26]      |
| $\text{Cu}_{0.8}\text{Ni}_{0.1}\text{Co}_{0.1} @ \text{MIL}-101$  | 72.1   | $T = 298 \text{ K}, n_{\text{AB}} = 1 \text{ mmol}, M_{\text{cat.}} = 50 \text{ mg}$           | [27]      |
| $\text{Cu}_{0.2}\text{Co}_{0.8}$ nanoparticles/RGO  | 50.6   | $T = 298 \text{ K}, n_{\text{AB}} = 1.3 \text{ mmol}, n_{\text{cat.}} = 0.065 \text{ mmol}$    | [28]      |
| $\text{Cu}@\text{MoCo}$ core–shell nanoparticles  | 49.6   | $T = 298 \text{ K}, n_{\text{AB}} = 2 \text{ mmol}, n_{\text{cat.}} = 0.08 \text{ mmol}$       | [29]      |
| $\text{Cu}(\text{OH})_2 @ \text{Co}_2\text{CO}_3(\text{OH})_2 / \text{CF}$  | 39.72  | $T = 298 \text{ K}, n_{\text{AB}} = 0.63 \text{ mmol}, n_{\text{cat.}} = 0.0055 \text{ mmol}$  | [30]      |
| $\text{Cu}-\text{Co}/\text{PDPA-HNTs}$  | 30.8   | $T = 298 \text{ K}, n_{\text{AB}} = 1.04 \text{ mmol}, V_{\text{cat.}} = 4 \text{ ml}$         | [31]      |
| $\text{CoCu}/\text{Ni}$ foam  | 30.5   | $T = 298 \text{ K}, n_{\text{AB}} = 2.6 \text{ mmol}, S_{\text{cat.}} = 5 \times 3 \text{ cm}$ | [32]      |
| $\text{CuCo}$   | 19.6   | $T = 298 \text{ K}, n_{\text{AB}} = 1 \text{ mmol}, M_{\text{cat.}} = 100 \text{ mg}$          | [33]      |
| $\text{Co}-\text{Cu}$ NWs   | 6.17   | $T = 298 \text{ K}, n_{\text{AB}} = 0.76 \text{ mmol}, M_{\text{cat.}} = 5 \text{ mg}$         | [34]      |
| $\text{Co}@\text{N-C-700}$  | 5.6  | $T = 298 \text{ K}, n_{\text{AB}} = 1.3 \text{ mmol}, M_{\text{cat.}} = 20 \text{ mg}$         | [35]      |
| $\text{Co}_{0.52}\text{Cu}_{0.48}$  | 3.4  | $T = 298 \text{ K}, n_{\text{AB}} = 0.16 \text{ mmol}, M_{\text{cat.}} = 29.7 \text{ mg}$      | [36]      |
| $\text{Cu}/\text{SiO}_2$  | 3.24   | $T = 298 \text{ K}, n_{\text{AB}} = 1 \text{ mmol}, n_{\text{cat.}} = 0.09 \text{ mmol}$       | [10]      |

In an industrial scale application, a catalyst with both high stability and good reusability is highly desired. The  $\text{H}_2$  evolution at different catalytic cycles in the case of the mixture of  $\text{Co}_3\text{O}_4$  and  $\text{Cu}_3(\text{MoO}_4)_2(\text{OH})_2$  with the mass ratio of 8:2 as the catalyst is displayed in Figure 3f. There is only a slight decrease in the activity for the mixture catalyst after five catalytic cycles. Moreover, the mole ratio of  $\text{H}_2/\text{AB}$  was still 3, which is indicative of complete hydrolytic conversion. These observations suggested that the mixture catalysts have good reusability and relatively high stability. The SEM images of the used mixture catalyst are shown in Figure S7, indicating that the microspheres ( $\text{Co}_3\text{O}_4$ ) and the nanoplate ( $\text{Cu}_3(\text{MoO}_4)_2(\text{OH})_2$ ) still exist in the sample. According to the following chemical equation:  $\text{NH}_3\text{BH}_3 + 2\text{H}_2\text{O} \rightarrow \text{NH}_4^+ + \text{BO}_2^- + 3\text{H}_2$ , the by-product of  $\text{BO}_2^-$  will be adsorbed on the surface of the catalysts and occupy some active sites, thus causing the slight decrease in the successive catalytic tests.

In a previous report, Cu(II) and Co(II) themselves were found to be inert toward  $\text{NH}_3\text{BH}_3$  hydrolysis [37]. However,  $\text{NH}_3\text{BH}_3$  in a reaction medium could reduce Cu(II) and Co(II) to metallic Cu and Co, which are the real active species for AB hydrolysis. Considering the relatively high standard reduction potential of  $\text{Cu}^{2+}/\text{Cu}$  (0.337 V vs. SHE) in contrast to that of  $\text{Co}^{3+}/\text{Co}$  (-0.28 V vs. SHE), Cu(II) can be reduced more readily than Co(II) [38]. Therefore, it is understandable that Cu-based catalysts can initiate  $\text{NH}_3\text{BH}_3$  hydrolysis instantly, while an induction time is needed in the case of Co-based catalysts.

Nevertheless, according to a study reported by Xu [39], Co shows better catalytic performance in  $\text{NH}_3\text{BH}_3$  dehydrogenation than Cu. So, the Co-based catalysts possess higher reactivity than Cu-based catalysts, as observed in Figure 3a.

As mentioned above, the formed Co(0) and Cu(0) reduced by AB are the real active species toward AB hydrolysis. To confirm the formation of Co(0) and Cu(0) in our catalyst, XPS analysis was performed on the used mixed catalyst of  $\text{Co}_3\text{O}_4$  and  $\text{Cu}_3(\text{MoO}_4)_2(\text{OH})_2$ . The results, presented in Figure 4a,b, show deconvoluted peaks at 793.8 and 778.6 eV in  $\text{Co}2\text{p}$ , as well as 952.9 and 932.9 eV in  $\text{Cu}2\text{p}$ , which correspond to Co(0) [40] and Cu(0) [23], respectively, thus demonstrating their formation. Accordingly, the formation rates of Co(0) and Cu(0) have a significant impact on the  $\text{H}_2$  production rate. In other words, the reducibility of Co- and Cu-based catalysts has an important effect on their catalytic activity toward AB hydrolysis. Therefore, the reducibility of  $\text{Co}_3\text{O}_4$ ,  $\text{Cu}_3(\text{MoO}_4)_2(\text{OH})_2$  and their mixture were characterized by  $\text{H}_2$ -TPR analysis. Figure 4c reveals that the TPR profile of  $\text{Co}_3\text{O}_4$  has two evident hydrogen consumption peaks centered at 287.6 and 387.5 °C. The two peaks are associated with the reduction of  $\text{Co}^{3+}$  to  $\text{Co}^{2+}$  and  $\text{Co}^{2+}$  to Co<sup>0</sup>, respectively [41]. The chemical equation can be expressed as follows:

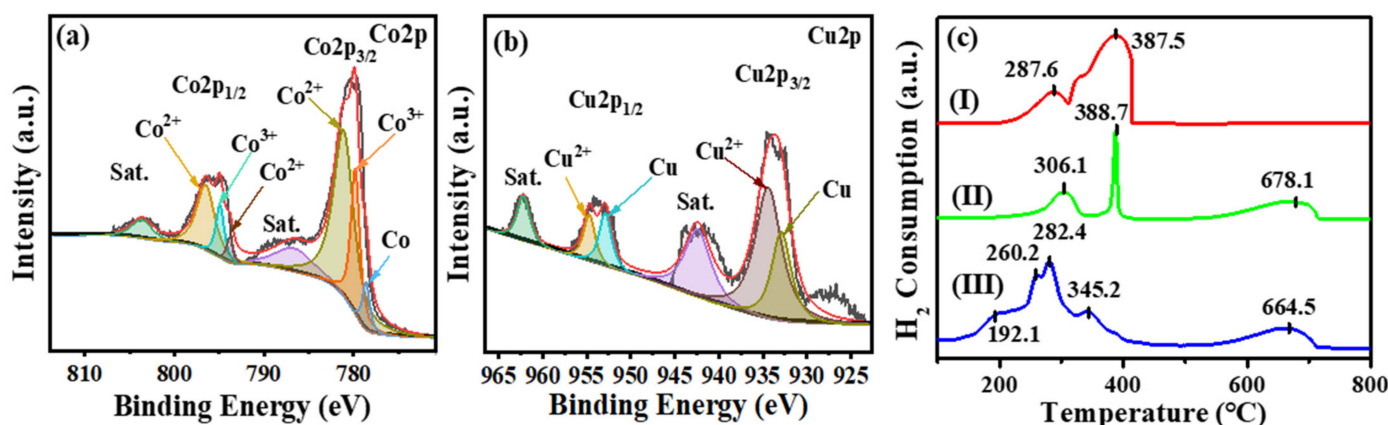
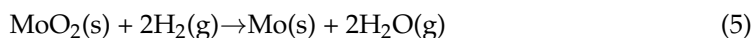
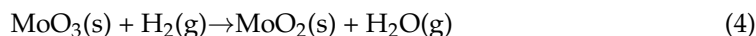


**Figure 4.** XPS spectra of used mixed catalyst of  $\text{Co}_3\text{O}_4$  and  $\text{Cu}_3(\text{MoO}_4)_2(\text{OH})_2$  (a,b) and  $\text{H}_2$ -TPR curves of  $\text{Co}_3\text{O}_4$  (I),  $\text{Cu}_3(\text{MoO}_4)_2(\text{OH})_2$  (II) and their mixture (III) (c).

The TPR profile of  $\text{Cu}_3(\text{MoO}_4)_2(\text{OH})_2$  has three strong reduction peaks. The first peak at about 306.1 °C is attributed to a copper oxide reduction ( $\text{Cu}(\text{II}) \rightarrow \text{Cu}(0)$ ) [22], and the higher temperature centered at 388.7 °C is indexed to the reduction process of Mo(VI) to Mo(IV) [22]. As the temperature increases to 678.1 °C, a broad peak appears, which is ascribed to the reduction of Mo(IV) to Mo(0) [23]. The reduction process of  $\text{Cu}_3(\text{MoO}_4)_2(\text{OH})_2$  is expressed as follows:



Remarkably, all the peaks in the TPR curve of the mixture of  $\text{Co}_3\text{O}_4$  and  $\text{Cu}_3(\text{MoO}_4)_2(\text{OH})_2$  shifted to a lower temperature under similar conditions compared to  $\text{Co}_3\text{O}_4$  and  $\text{Cu}_3(\text{MoO}_4)_2(\text{OH})_2$ , which further confirms that the mixture can be more easily reduced. The decreased reduction temperature may be caused by the active intermediate Cu-H species, which is formed during the reduction of the Cu species by hydrogen. The active intermediate Cu-H possesses very strong reducibility [25]. When they come into contact

with  $\text{Cu}_3(\text{MoO}_4)_2(\text{OH})_2$  or  $\text{Co}_3\text{O}_4$ , they can easily reduce  $\text{Cu}_3(\text{MoO}_4)_2(\text{OH})_2$  or  $\text{Co}_3\text{O}_4$  to the counterparts with zero valence. Thus, the active metallic Cu and Co are formed and immediately act as catalysts to hydrolyze  $\text{NH}_3\text{BH}_3$ . In this case, the catalytic activity of the mixture is markedly improved.

### 3. Materials and Methods

#### 3.1. Preparation of Samples

In the preparation of the  $\text{Co}_3\text{O}_4$  hollow microsphere, a mixture solution of 2.0 mmol  $\text{Co}(\text{NO}_3)_2 \cdot 6\text{H}_2\text{O}$  (Aladdin, 99%) and 2.0 mmol potassium sodium tartrate tetrahydrate ( $\text{C}_4\text{H}_4\text{O}_6\text{KNa} \cdot 4\text{H}_2\text{O}$ , Taishan Yueqiao Reagent Plastic Co. Ltd., Jiangmen, China, >99%) were prepared in deionized water (40.0 mL) under stirring. Then, 40 mL of a 0.125 M  $\text{NaHCO}_3$  (Sinopharm Chemical Reagent Co. Ltd., Shanghai, China, ≥99.5%) solution was added into the above solution drop by drop. Stirring for half an hour, the mixed solution was poured into a Teflon-lined autoclave (100 mL), sealed and heated to 120 °C for 8 h. After the reaction, the final product was thoroughly rinsed with ethanol and deionized water and subsequently calcined at 500 °C for 2 h.

In the preparation of the  $\text{Cu}_3(\text{MoO}_4)_2(\text{OH})_2$  nanoplate, an aqueous solution (40 mL) containing 4 mmol  $\text{CuCl}_2$  (Taishan Yueqiao Reagent Plastic Co. Ltd., >99 %) was prepared. Subsequently, 40 mL of 0.1 M  $\text{Na}_2\text{MoO}_4$  (Tianjin Damao Chemical Reagent Co. Ltd., Tianjin, China, >99%) solution was dropped into the  $\text{CuCl}_2$  solution. The resultant solution was hydrothermally heated at 120 °C for 8 h. The final product was flushed thoroughly with ethanol and deionized water. Finally, the sample was dehydrated in air at 80 °C for 6 h. The synthetic processes for  $\text{Co}_3(\text{PO}_4)_2$ ,  $\text{Cu}_3(\text{PO}_4)_2$ , and  $\text{CuO}$  can be seen in the supporting information.

#### 3.2. Characterization

Powder X-ray diffraction (XRD) patterns were obtained on a Rigaku Ultima IV diffractometer (Rigaku Corporation, Kyoto, Japan) with  $\text{Cu K}\alpha$  radiation ( $\lambda = 1.5406 \text{ \AA}$  at 40 kV and 40 mA). The morphology of the catalysts was investigated by scanning electron microscopy (SEM) using a Hitachi Su-8010 scanning electron microscope (Hitachi Ltd., Tokyo, Japan). Transmission electron microscopy (TEM) and high-resolution TEM (HRTEM) images were obtained using an FEI Tecnai G2 F20 S-TWIN transmission electron microscope (FEI Company, Hillsboro, OR, USA). X-ray photoelectron spectroscopy (XPS) spectra were recorded on a Kratos Axis Ultra DLD X-ray photoelectron spectrometer (Kratos Analytical Ltd., Manchester, UK) with  $\text{Al K}\alpha$  radiation. A Micromeritics ASAP 2020 nitrogen adsorption analyzer (Micromeritics Instruments, Norcross, GA, USA) was used to obtain the nitrogen adsorption–desorption isotherms and the Brunauer–Emmett–Teller (BET) surface areas of the samples. Fourier transform infrared (FTIR) spectroscopy analysis was performed on a Bruker Tensor 27 FTIR spectrometer (Bruker Optik GmbH, Ettlingen, Germany) to obtain the FTIR spectra of the samples.

#### 3.3. Hydrogen Production Experiments

The hydrogen production experiment was performed in a round-bottom flask sealed and connected to a glass burette. Unless specified, the catalytic activity was measured at 25 °C. The reaction flask was placed in a water bath to maintain the temperature at 25 °C under an ambient atmosphere. Typically, the catalyst (10.0 mg) was ultrasonically dispersed in deionized water (10 mL). Afterwards, a 10 mL mixed solution of  $\text{NH}_3\text{BH}_3$  (0.3 M) and  $\text{NaOH}$  (2 M) was quickly injected into the round-bottom flask. The reaction time counting was started when the first bubble appeared. The volume of the generated gas could be monitored by recording the displacement of water in the gas burette. The experimental set-up for hydrolysis can be seen in Figure S1 in the Supplementary Materials.

#### 4. Conclusions

In this study, a universal, simple and efficient strategy for enhancing catalytic activity toward AB hydrolysis is proposed. By simply mixing Co- and Cu-based compounds, synergistic catalysts with markedly enhanced catalytic activity can be obtained. We evaluated the catalytic performance of five couples of catalysts in AB hydrolysis. The results revealed that the activity of the mixture catalysts was much higher than the sum of that of the activity of the individual compounds. In particular, the mixture of  $\text{Cu}_3(\text{MoO}_4)_2(\text{OH})_2$  and  $\text{Co}_3\text{O}_4$  at the mass ratio of 8:2 exhibited a robust catalytic performance with a TOF of  $77.3 \text{ min}^{-1}$ , which is one of the most active non-precious-metal-based catalysts ever reported in the literature. The reason for the enhancement of the activity of the mixture catalysts is believed to be closely related to their enhanced reducibility. The findings in this work provide a guideline for promoting  $\text{NH}_3\text{BH}_3$  hydrolysis through a simple and effective approach.

**Supplementary Materials:** The following supporting information can be downloaded at: <https://www.mdpi.com/article/10.3390/catal12040426/s1>, Preparation of  $\text{Co}_3(\text{PO}_4)_2$ ,  $\text{Cu}_3(\text{PO}_4)_2$  and  $\text{CuO}$ ; Figure S1: Illustration of the set-up for the hydrolysis experiments; Figure S2: SEM images of  $\text{Co}_3(\text{PO}_4)_2$  (a,b),  $\text{CuO}$  (d,e) and  $\text{Cu}_3(\text{PO}_4)_2 \cdot 3\text{H}_2\text{O}$  (g,h), and XRD patterns of  $\text{Co}_3(\text{PO}_4)_2$  (c),  $\text{CuO}$  (f) and  $\text{Cu}_3(\text{PO}_4)_2 \cdot 3\text{H}_2\text{O}$  (i); Figure S3: FT-IR spectra of  $\text{Co}_3(\text{PO}_4)_2$  (a),  $\text{CuO}$  (b) and  $\text{Cu}_3(\text{PO}_4)_2$  (c); Figure S4: Catalytic performance of mixtures of Co- and Cu-based catalysts with various mass ratios and the comparison of their TOF values:  $\text{Co}_3\text{O}_4$  and  $\text{Cu}_3(\text{PO}_4)_2$  (a,b),  $\text{Co}_3(\text{PO}_4)_2$  and  $\text{Cu}_3(\text{MoO}_4)_2(\text{OH})$  (c,d),  $\text{Co}_3(\text{PO}_4)_2$  and  $\text{Cu}_3(\text{PO}_4)_2$  (e,f),  $\text{Co}_3\text{O}_4$  and  $\text{CuO}$  (g,h); Figure S5: XPS spectra in Co 2p and P 2p regions (a,b), elemental mapping (c) and H<sub>2</sub>-TPR profile (d) of  $\text{Co}_3(\text{PO}_4)_2$ ; Figure S6: Catalytic performance of mixture of Co- and Cu-based catalyst with various mass ratio and the comparison of their TOF Value:  $\text{Co}_3\text{O}_4$  and  $\text{Cu}_3(\text{PO}_4)_2$  (a,b),  $\text{Co}_3(\text{PO}_4)_2$  and  $\text{Cu}_3(\text{MoO}_4)_2(\text{OH})$  (c,d),  $\text{Co}_3(\text{PO}_4)_2$  and  $\text{Cu}_3(\text{PO}_4)_2$  (e,f),  $\text{Co}_3\text{O}_4$  and  $\text{CuO}$  (g,h); Figure S7: Low-magnification (a) and high-magnification (b) SEM images of the catalysts after 5th catalytic run. The  $\text{Co}_3\text{O}_4$  microspheres and  $\text{Cu}_3(\text{MoO}_4)_2(\text{OH})_2$  nanoplates in Figure S7b are marked with blue circles and yellow rectangles, respectively.

**Author Contributions:** Conceptualization, J.L. (Jinyun Liao), Y.W. and Y.F.; methodology, J.L. (Jinyun Liao), Y.W., H.H. and L.Z.; investigation, J.L. (Jinyun Liao), Y.W., H.H., L.Z. and J.Q.; data curation, J.L. (Junhao Li) and Y.W.; writing—original draft preparation, J.L. (Jinyun Liao); writing—review and editing, Q.L. and H.L.; supervision, Q.L.; project administration, H.L. All authors have read and agreed to the published version of the manuscript.

**Funding:** This work was supported by the Key-Area Research and Development Program of Guangdong Province (No. 2020B090919005), the National Natural Science Foundation of China (Nos. U1801257, 21975056), the Major and Special Project in the Field of Intelligent Manufacturing of the Universities in Guangdong Province (No. 2020ZDZX2067), Pearl River Science and Technology New Star Project (No. 201806010039), the Science & Technology project of Huizhou City (No. 2020SD0404032), the Natural Science Foundation of Huizhou University (No. 20180927172750326), and the Professorial and Doctoral Scientific Research Foundation of Huizhou University (Nos. 2018JB036, 2019JB023 and 2019JB034).

**Data Availability Statement:** The data presented in this study are available in Supplementary Materials.

**Conflicts of Interest:** The authors declare no conflict of interest.

#### References

1. Zhao, D.L.; Han, Z.G.; Huo, T.T.; Yuan, Z.M.; Qi, Y.; Zhang, Y.H. Advances in activation property of hydrogen storage for TiFe-based alloy. *Chin. J. Rare Metals* **2020**, *44*, 337–351.
2. Qin, P.L.; Zeng, K.; Lan, Z.Q.; Huang, X.T.; Liu, H.Z.; Guo, J. Enhanced hydrogen storage properties of Mg-Al alloy catalyzed with reduced graphene oxide supported with LaClO. *Chin. J. Rare Metals* **2020**, *44*, 499–507.
3. Alpaydin, C.Y.; Gulbay, S.K.; Colpan, C.O. A review on the catalysts used for hydrogen production from ammonia borane. *Int. J. Hydron. Energy* **2019**, *45*, 3414–3434. [[CrossRef](#)]
4. Wu, H.; Cheng, Y.; Fan, Y.; Lu, X.; Li, L.; Liu, B.; Li, B.; Lu, S. Metal-catalyzed hydrolysis of ammonia borane: Mechanism, catalysts, and challenges. *Int. J. Hydron. Energy* **2020**, *45*, 30325–30340. [[CrossRef](#)]
5. Rakap, M.; Kalu, E.; Özkar, S. Hydrogen generation from hydrolysis of ammonia-borane using Pd-PVB-TiO<sub>2</sub> and Co-Ni-P/Pd-TiO<sub>2</sub> under stirred conditions. *J. Power Sources* **2012**, *210*, 184–190. [[CrossRef](#)]

6. Aksoy, M.; Metin, Ö. Pt nanoparticles supported on mesoporous graphitic carbon nitride as catalysts for hydrolytic dehydrogenation of ammonia borane. *ACS Appl. Nano Mater.* **2020**, *3*, 6836–6846. [[CrossRef](#)]
7. Li, Y.T.; Zhang, X.L.; Peng, Z.K.; Liu, P.; Zheng, X.C. Highly efficient hydrolysis of ammonia borane using ultrafine bimetallic RuPd nanoalloys encapsulated in porous g-C<sub>3</sub>N<sub>4</sub>. *Fuel* **2020**, *277*, 118243–118253. [[CrossRef](#)]
8. Guo, K.; Ding, Y.; Luo, J.; Gu, M.; Yu, Z. NiCu bimetallic nanoparticles on silica support for catalytic hydrolysis of ammonia borane: Composition-dependent activity and support size effect. *ACS Appl. Energy Mater.* **2019**, *2*, 5851–5861. [[CrossRef](#)]
9. Wang, C.; Li, L.; Yu, X.; Lu, Z.; Zhang, X.; Wang, X.; Yang, X.; Zhao, J. Regulation of d-band electrons to enhance the activity of Co-based non-noble bimetal catalysts for hydrolysis of ammonia borane. *ACS Sustain. Chem. Eng.* **2020**, *8*, 8256–8266. [[CrossRef](#)]
10. Yao, Q.; Lu, Z.H.; Zhang, Z.; Chen, X.; Lan, Y. One-pot synthesis of core-shell Cu@SiO<sub>2</sub> nanospheres and their catalysis for hydrolytic dehydrogenation of ammonia borane and hydrazine borane. *Sci. Rep.* **2014**, *4*, 7597–7604. [[CrossRef](#)] [[PubMed](#)]
11. Feng, K.; Zhong, J.; Zhao, B.; Zhang, H.; Xu, L.; Sun, X.; Lee, S.-T. Cu<sub>x</sub>Co<sub>1-x</sub>O nanoparticles on graphene oxide as a synergistic catalyst for high-efficiency hydrolysis of ammonia–borane. *Angew. Chem. Int. Ed.* **2016**, *55*, 11950–11954. [[CrossRef](#)] [[PubMed](#)]
12. Liao, J.; Lu, D.; Diao, G.; Zhang, X.; Zhao, M.; Li, H. Co<sub>0.8</sub>Cu<sub>0.2</sub>MoO<sub>4</sub> microspheres composed of nanoplatelets as a robust catalyst for the hydrolysis of ammonia borane. *ACS Sustain. Chem. Eng.* **2018**, *6*, 5843–5851. [[CrossRef](#)]
13. Yamada, Y.; Yano, K.; Fukuzumi, S. Catalytic application of shape-controlled Cu<sub>2</sub>O particles protected by Co<sub>3</sub>O<sub>4</sub> nanoparticles for hydrogen evolution from ammonia borane. *Energy Environ. Sci.* **2012**, *5*, 5356–5363. [[CrossRef](#)]
14. Feng, Y.; Zhu, Y.; Li, Y.; Li, L.; Lv, F.; Li, Z.; Li, H.; He, M. Co<sub>3x</sub>Cu<sub>3-3x</sub>(PO<sub>4</sub>)<sub>2</sub> microspheres, a novel non-precious metal catalyst with superior catalytic activity in hydrolysis of ammonia borane for hydrogen production. *Int. J. Hydrol. Energy* **2020**, *45*, 17444–17452. [[CrossRef](#)]
15. Katkar, P.K.; Marje, S.J.; Pujari, S.S.; Khalate, S.A.; Lokhande, A.C.; Patil, U.M. Enhanced energy density of all-solid-state asymmetric supercapacitors based on morphologically tuned hydrous cobalt phosphate electrode as cathode material. *ACS Sustain. Chem. Eng.* **2019**, *7*, 11205–11218. [[CrossRef](#)]
16. Feng, Y.; Zhang, J.; Ye, H.; Wang, H.; Li, X.; Zhang, X.; Li, H. Ni<sub>0.5</sub>Cu<sub>0.5</sub>Co<sub>2</sub>O<sub>4</sub> nanocomposites, morphology, controlled synthesis, and catalytic performance in the hydrolysis of ammonia borane for hydrogen production. *Nanomaterials* **2019**, *9*, 1334. [[CrossRef](#)]
17. Kianpour, G.; Salavati-Niasari, M.; Emadi, H. Precipitation synthesis and characterization of cobalt molybdates nanostructures. *Superlattice Microstruct.* **2013**, *58*, 120–129. [[CrossRef](#)]
18. Umapathy, V.; Neeraja, P. Sol–gel synthesis and characterizations of CoMoO<sub>4</sub> nanoparticles: An efficient photocatalytic degradation of 4-chlorophenol. *J. Nanosci. Nanotechnol.* **2016**, *16*, 2960–2966. [[CrossRef](#)]
19. Swain, B.; Lee, D.-H.; Park, J.; Lee, C.-G.; Lee, K.-J.; Kim, D.-W.; Park, K.-S. Synthesis of Cu<sub>3</sub>(MoO<sub>4</sub>)<sub>2</sub>(OH)<sub>2</sub> nanostructures by simple aqueous precipitation: Understanding the fundamental chemistry and growth mechanism. *CrystEngComm* **2017**, *19*, 154–165. [[CrossRef](#)]
20. Zhang, Y.; Wang, S.; Li, X.; Chen, L.; Qian, Y.; Zhang, Z. CuO shuttle-like nanocrystals synthesized by oriented attachment. *J. Cryst. Growth* **2006**, *291*, 196–201. [[CrossRef](#)]
21. Gao, J.; Liu, H.; Pang, L.; Guo, K.; Li, J. Biocatalyst and colorimetric/fluorescent dual biosensors of H<sub>2</sub>O<sub>2</sub> constructed via hemoglobin–Cu<sub>3</sub>(PO<sub>4</sub>)<sub>2</sub> organic/inorganic hybrid nanoflowers. *ACS Appl. Mater. Interfaces* **2018**, *10*, 30441–30450. [[CrossRef](#)]
22. Yuan, M.; Yang, Y.; Nan, C.; Sun, G.; Li, H.; Ma, S. Porous Co<sub>3</sub>O<sub>4</sub> nanorods anchored on graphene nanosheets as an effective electrocatalysts for aprotic Li–O<sub>2</sub> batteries. *Appl. Surf. Sci.* **2018**, *444*, 312–319. [[CrossRef](#)]
23. Lu, D.; Liao, J.; Li, H.; Ji, S.; Pollet, B. Co<sub>3</sub>O<sub>4</sub>/CuMoO<sub>4</sub> hybrid microflowers composed of nanorods with rich particle boundaries as a highly active catalyst for ammonia borane hydrolysis. *ACS Sustain. Chem. Eng.* **2019**, *7*, 16474–16482. [[CrossRef](#)]
24. Lu, D.; Liao, J.; Zhong, S.; Leng, Y.; Ji, S.; Wang, H.; Wang, R.; Li, H. Cu<sub>0.6</sub>Ni<sub>0.4</sub>Co<sub>2</sub>O<sub>4</sub> nanowires, a novel noble-metal-free catalyst with ultrahigh catalytic activity towards the hydrolysis of ammonia borane for hydrogen production. *Int. J. Hydrol. Energy* **2018**, *43*, 5541–5550. [[CrossRef](#)]
25. Lu, D.; Li, J.; Lin, C.; Liao, J.; Feng, Y.; Ding, Z.; Li, Z.; Liu, Q.; Li, H. A simple and scalable route to synthesize Co<sub>x</sub>Cu<sub>1-x</sub>Co<sub>2</sub>O<sub>4</sub>@Co<sub>y</sub>Cu<sub>1-y</sub>Co<sub>2</sub>O<sub>4</sub> yolk–shell microspheres, a high-performance catalyst to hydrolyze ammonia borane for hydrogen production. *Small* **2019**, *15*, 1805460–1805468. [[CrossRef](#)]
26. Liao, J.; Feng, Y.; Wu, S.; Ye, H.; Zhang, J.; Zhang, X.; Xie, F.; Li, H. Hexagonal CuCo<sub>2</sub>O<sub>4</sub> nanoplatelets, a highly active catalyst for the hydrolysis of ammonia borane for hydrogen production. *Nanomaterials* **2019**, *9*, 360. [[CrossRef](#)] [[PubMed](#)]
27. Liang, Z.; Xiao, X.; Yu, X.; Huang, X.; Jiang, Y.; Fan, X.; Chen, L. Non-noble trimetallic Cu–Ni–Co nanoparticles supported on metal–organic frameworks as highly efficient catalysts for hydrolysis of ammonia borane. *J. Alloy. Compd.* **2018**, *741*, 501–508. [[CrossRef](#)]
28. Xu, M.; Huai, X.; Zhang, H. Highly dispersed CuCo nanoparticles supported on reduced graphene oxide as high-activity catalysts for hydrogen evolution from ammonia borane hydrolysis. *J. Nanopart. Res.* **2018**, *20*, 329–341. [[CrossRef](#)]
29. Wang, C.; Wang, H.; Wang, Z.; Li, X.; Chi, Y.; Wang, M.; Gao, D.; Zhao, Z. Mo remarkably enhances catalytic activity of Cu@MoCo core–shell nanoparticles for hydrolytic dehydrogenation of ammonia borane. *Int. J. Hydrol. Energy* **2018**, *43*, 7347–7355. [[CrossRef](#)]
30. Wang, J.; Ma, X.; Yang, W.; Sun, X.; Liu, J. Self-supported Cu(OH)<sub>2</sub>@Co<sub>2</sub>CO<sub>3</sub>(OH)<sub>2</sub> core–shell nanowire array as a robust catalyst for ammonia–borane hydrolysis. *Nanotechnology* **2017**, *28*, 045606–045611. [[CrossRef](#)]
31. Liu, Y.; Zhang, J.; Guan, H.; Zhao, Y.; Yang, J.H.; Zhang, B. Preparation of bimetallic Cu–Co nanocatalysts on poly (diallyldimethylammonium chloride) functionalized halloysite nanotubes for hydrolytic dehydrogenation of ammonia borane. *Appl. Surf. Sci.* **2018**, *427*, 106–113. [[CrossRef](#)]

32. Liao, J.; Lv, F.; Feng, Y.; Zhong, S.; Wu, X.; Zhang, X.; Wang, H.; Li, J.; Li, H. Electromagnetic-field-assisted synthesis of Ni foam film-supported CoCu alloy microspheres composed of nanosheets: A high performance catalyst for the hydrolysis of ammonia borane. *Catal. Commun.* **2019**, *122*, 16–19. [[CrossRef](#)]
33. Li, J.; Zhu, Q.-L.; Xu, Q. Non-noble bimetallic CuCo nanoparticles encapsulated in the pores of metal–organic frameworks: Synergetic catalysis in the hydrolysis of ammonia borane for hydrogen generation. *Catal. Sci. Technol.* **2015**, *5*, 525–530. [[CrossRef](#)]
34. Sun, L.; Li, X.; Xu, Z.; Xie, K.; Liao, L. Synthesis and catalytic application of magnetic Co–Cu nanowires. *Beilstein J. Nanotechnol.* **2017**, *8*, 1769–1773. [[CrossRef](#)]
35. Wang, H.; Zhao, Y.; Cheng, F.; Tao, Z.; Chen, J. Cobalt nanoparticles embedded in porous N-doped carbon as long-life catalysts for hydrolysis of ammonia borane. *Catal. Sci. Technol.* **2016**, *6*, 3443–3448. [[CrossRef](#)]
36. Sang, W.; Wang, C.; Zhang, X.; Yu, X.; Yu, C.; Zhao, J.; Wang, X.; Yang, X.; Li, L. Dendritic  $\text{Co}_{0.52}\text{Cu}_{0.48}$  and  $\text{Ni}_{0.19}\text{Cu}_{0.81}$  alloys as hydrogen generation catalysts via hydrolysis of ammonia borane. *Int. J. Hydrot. Energy* **2017**, *42*, 30691–30703.
37. Kalidindi, S.; Sanyal, U.; Jagirdar, B. Nanostructured Cu and Cu@ $\text{Cu}_2\text{O}$  core shell catalysts for hydrogen generation from ammonia–borane. *Phys. Chem. Chem. Phys.* **2008**, *10*, 5870–5874. [[CrossRef](#)] [[PubMed](#)]
38. Lu, Z.-H.; Li, J.; Feng, G.; Yao, Q.; Zhang, F.; Zhou, R.; Tao, D.; Chen, X.; Yu, Z. Synergistic catalysis of MCM-41 immobilized Cu–Ni nanoparticles in hydrolytic dehydrogenation of ammonia borane. *Int. J. Hydrot. Energy* **2014**, *39*, 13389–13395. [[CrossRef](#)]
39. Xu, Q.; Chandra, M. Catalytic activities of non-noble metals for hydrogen generation from aqueous ammonia–borane at room temperature. *J. Power Sources* **2006**, *163*, 364–370. [[CrossRef](#)]
40. Wei, Z.; Wang, J.; Mao, S.; Su, D.; Jin, H.; Wang, Y.; Xu, F.; Li, H.; Wang, Y. In situ-generated  $\text{Co}^0\text{-Co}_3\text{O}_4/\text{N}$ -doped carbon nanotubes hybrids as efficient and chemoselective catalysts for hydrogenation of nitroarenes. *ACS Catal.* **2015**, *5*, 4783–4789. [[CrossRef](#)]
41. Ma, X.; Yu, X.; Yang, X.; Lin, M.; Ge, M. Hydrothermal synthesis of a novel double-sided nanobrush  $\text{Co}_3\text{O}_4$  catalyst and its catalytic performance for benzene oxidation. *ChemCatChem* **2019**, *11*, 1214–1221. [[CrossRef](#)]